Physica Scripta

PAPER

Theoretical investigations of optoelectronic and transport properties of halide based K_2YAuX_6 (X = Cl, Br) double perovskites

Ghulam M Mustafa[1,*], **Raja Waqar**[2], **Sadaf Saba**[3], **N A Noor**[4], **Zahid Farooq**[1], **Muhammad Imran**[5], **R B Behram**[6] **and Yousef Mohammed Alanazi**[7]

[1] Department of Physics, Division of Science and Technology, University of Education, Lahore, Punjab 54770, Pakistan
[2] Electrical and Biological Physics, Krangwoon University, Seoul, 01897, Republic of Korea
[3] Department of Physics, Government College University, Faisalabad, 38040, Pakistan
[4] Department of Physics, RIPHAH International University, Campus Lahore, Pakistan
[5] Department of Physics, Government College University, Lahore, Pakistan
[6] Department of Physics, AIOU, Islamabad, Pakistan
[7] College of Engineering, Chemical Engineering Department, King Saud University Riyadh, Saudi Arabia
[*] Author to whom any correspondence should be addressed.

E-mail: dr.ghulam.muhammad@ue.edu.pk

RECEIVED
23 November 2022

REVISED
29 April 2023

ACCEPTED FOR PUBLICATION
5 May 2023

PUBLISHED
23 May 2023

Keywords: double perovskites, tolerance factor, enthalpy of formation, band structure

Abstract

Intriguing optoelectronic and transport properties with huge compositional range and structural stability make double perovskites interesting for energy harvesting technologies. Here we theoretically investigate the structural, optical, mechanical, and transport properties of K2YAuX6 (X = Cl, Br) double perovskites using the WIEN2K code. Based on the calculated values of the tolerance factor and enthalpy of production, the thermodynamic and structural stability is affirmed. The ductile nature of these compositions is revealed in the computation of Poisson's ratio (>0.26) and Pugh's (1.75) ratio. The involvement of s-states of K, p-states of Cl/Br, and d-states of Y and Au in the formation of valence and conduction band edges is exhibited from the density of state plots. Using the Tran-Blaha mBJ potential and spin-orbital coupling, the energy bandgap value for K2YAuCl6 and K2YAuBr6 is reported as 3.20, and 2.70 eV, respectively, which is suitable for the fabrication of light-emitting diodes. Optical behavior is further explored regarding complex dielectric constant, refractive index, optical conductivity, optical loss, and absorption factor. The small value of thermal conductivity with large value of electrical conductivity, Seebeck coefficient, power factor, and figure of merit revealed the potential of these materials for the fabrication of light-emitting diodes and thermoelectric generators.

1. Introduction

Efficient utilization of energy is a crucial aspect of modern civilization and its evolution [1]. Most of the energy we use comes from the burning of solid fuels. This usage of fossil fuels contains major issues such as climate change and global warming [2]. It is worth noticing that only one-third of generated energy is effectively utilized, whereas rest two-thirds is wasted as heat [3]. So, there is an urgency to develop such devices that can proficiently convert this wasted heat into useful energy [4]. Developing a device that can convert the wasted heat of automobiles, residential, and industrial heating processes to electrical energy is highly desired [5–7]. Thermoelectric (TE) materials can transform wasted heat into electrical energy and gained considerable attention. The Seebeck effect is a key parameter in analyzing the efficiency of TE materials [8, 9]. The promising solid-state nature of TE materials make them flexible in operational integration [10]. The efficiency of these materials is calculated using the expression $ZT = S^2\sigma T/\kappa$. In this expression, T, σ, κ, and S are absolute temperature, electrical, thermal conductivity, and Seebeck coefficient, respectively [11, 12]. The motion of electron in response to temperature gradient constitute to the electronic part of thermal conductivity (κ_e) and temperature dependent lattice vibration is called lattice thermal conductivity (κ_l) combinedly define the net thermal conductivity of the material. For better thermoelectric performance, the electrical conductivity and

Seebeck coefficient should be large and thermal conductivity should be small [13, 14]. The fundamental issue regarding improvement of thermoelectric performance is the implicit nature of involving quantities which leads to the interesting fact that increasing one quantity reduces the other [15].

Most of the thermoelectric materials in service are chalcogenides like Bi_2Se_3, Bi_2Te_3, Sb_2Te_3, and Zn_4Sb_3 [16]. The major heat produces from several sources is at more than 900 K temperature, where these materials are decomposed or oxidized [17]. Thus halide-based double perovskite materials are strong candidates for high-temperature thermoelectric applications owing to their low cost, easy availability of constituent elements, and thermal stability at high temperature [18]. The general formula of these materials is $A_2B'B''X_6$. In this expression, *A* is usually an alkali metal, *B′* and *B″* are transition metals, and *X* is a halide anion [19]. In the crystal structure of double perovskites (DP) there are three types of cationic arrangement of *B*-site atoms i.e., layered, rock salt, and random, which can be distinguished based on the ordering of $B'X_6$ and $B''X_6$ octahedra [20]. This different arrangement of octahedra generates different geometry and thus, different space groups. The space group belonging to the random arrangement of octahedra is $Pm\bar{3}m$ [21]. In this arrangement, *A*-site divalent atoms with coordinates (0, 0, 0) occupy the corner positions, whereas tetravalent *B′* and *B″* occupy the body-centered position (1/2, 1/2, 1/2) whereas halide ions take a face-centered positions (0, 1/2, 1/2). In rock salt arrangement, $B'X_6$ and $B''X_6$ octahedra arrange alternately in three-dimensional space and thus give birth to three different space groups: *P4/nmc*, $Fd\bar{3}m$ and *I4/m* [22–24]. The layered-type structure of DP is the least common and rarely studied in which $B'X_6$ and $B''X_6$ octahedra are alternatively arranged in one dimension [25]. The stability of developed double perovskites can be predicted by computing the Goldschmidt tolerance factor. For stable double perovskites, the value of T_F should be in the range of 0.9 to 1.4 [26].

Double perovskites have huge structural flexibility and thus can accommodate various cations at cation sites, thus giving them a wide range of applications. The DP with halides as an anion were broadly studied for their optoelectronic and thermoelectric applications [27, 28]. For instance, Kangsabanik *et al* conducted an intuitive analysis of double perovskites and proposed that double perovskites effectively replace simple perovskites because of their better light-to-electricity conversion efficiency with improved stability [29]. This statement received further support from the study of Chakraborty *et al* who suggested that DPs are taking more place in the photovoltaic market due to their higher stability and scalability [30]. In addition, Slavney *et al* synthesized $Cs_2AgBiBr_6$ DPs and studied its optoelectronic properties, and observed that this composition has an indirect bandgap nature with an appropriate bandgap value [31]. Similarly, Volonasik *et al* theoretically and experimentally evaluated $Cs_2InAgCl_6$ composition and observed its bandgap value of 3.3 eV. They proposed that this bandgap can be modified by suitable adjusting the halide ions [32]. The compositions with wide bandgap having indirect nature are not suitable for solar cell applications, and recently, Meng *et al* claimed that due to the presence of inversion symmetry, indirect bandgap compositions are not optically transition free [33].

However, among the available compositions, $Cs_2(Ti, In)^{+1}(Bi, Sb)^{+3}X_6$ are the rare compositions that evolved due to extensive research work on double perovskites. During the comprehensive literature survey, we did not come across any study on the thermoelectric characteristics of K_2YAuX_6 (Cl, Br); thus, we planned to explore the potential of these double perovskite compositions for emerging technological applications thus, in this study, we elaborated the structural, optoelectronic and thermoelectric applications of these compositions and we believe that this writing would add a piece of substantial information in the existing knowledge regarding DPs and would unveil the underlying mechanism in working of thermoelectric devices.

2. Computational

Within the WIEN2K computational package, the full-potential linearized augmented plane wave method (FP-LAPW) developed on the basis of density functional theory (DFT) was implemented to compute the optoelectronic and thermoelectric properties of double perovskites [34–36]. The electronic structure was checked by the optimization of the cubic phase and space group as well as ground state lattice constant and bulk modulus. The ground state behavior was calculated using the Birch-Murnaghan equations of state that used energy released during the optimization process [37]. The PBEsol-GGA measured the ground state parameters accurately and mBJ potential generate bandgap values close to experimental value. In K_2YAuCl/Br_6 DPs, the electronic bandgaps were estimated using TB-mBJ potential [38, 39]. The values of the product of R_{MT} and K_{max}, G_{max}, and k-mesh were kept constant at 8, 16, and 1000. To get more reliable value of bandgap, k-mesh was made denser to by increasing the number of k-points. These optical factors were calculated with the help of the Kramer-Kronig relation [40]. For different types of materials, the BoltzTraP code of classical transport theory has been used to explore the thermoelectric factors, that's why we also utilized this approach here [41, 42].

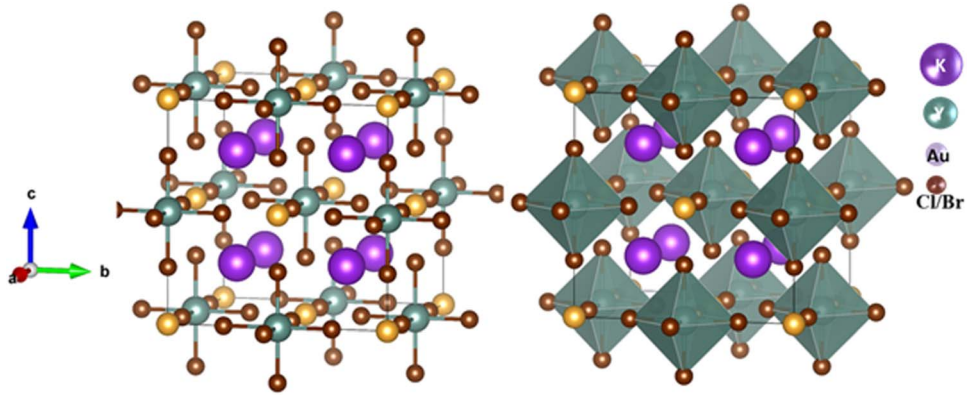

Figure 1. Crystal structure plot of double perovskites K_2YAuCl_6 and K_2YAuBr_6 halides.

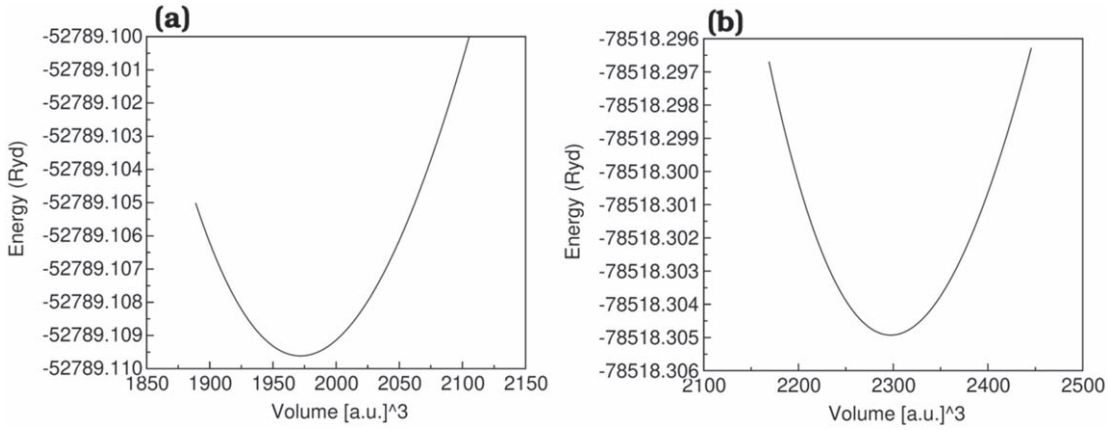

Figure 2. Optimization plot of investigated double perovskites (a) $K_2ScAuCl_6$ and (b) $K_2ScAuBr_6$ halides.

Table 1. Calculated values of lattice constant a_o(Å) compared with existing work, bulk modulus B_o(GPa), Enthalpy of formation (ΔH_f) and elastic parameters of K_2YAuCl_6 and K_2YAuBr_6 halides.

Parameters	K_2YAuCl_6	K_2YAuBr_6
	PBEsol-GGA	PBEsol-GGA
a_o(Å)	10.53	11.08
Other work	10.74[a]	11.28
B_o (*GPa*)	35.52	30.03
ΔH_f	−2.08	−1.56
C_{11}	86.54	59.99
C_{12}	10.89	15.12
C_{44}	7.65	8.07
B	35.44	30.07
G	15.29	12.33
Y	40.11	32.54
B/G	2.31	2.43
υ	0.31	0.31
A	0.20	0.35

[a] [46].

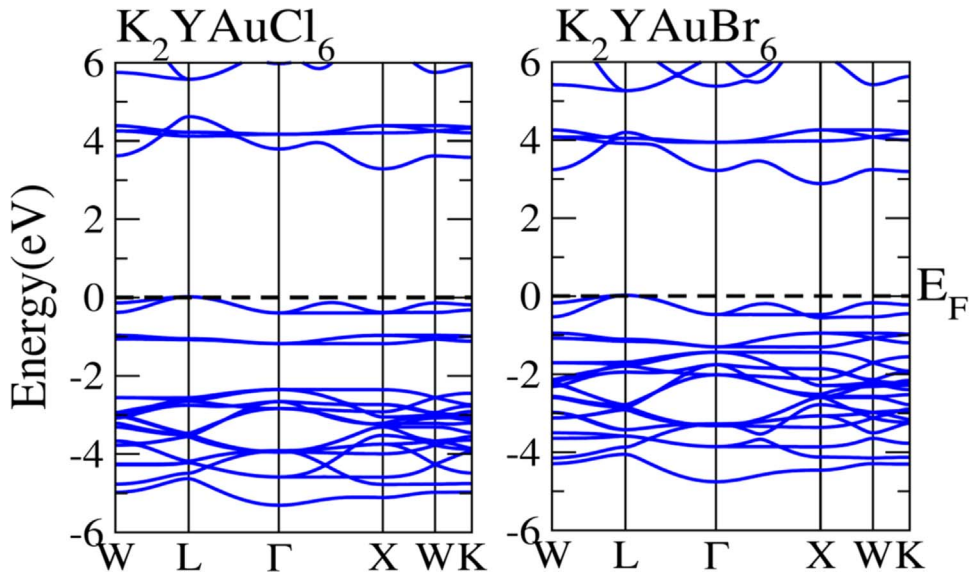

Figure 3. Calculated electronic band structure for K_2YAuCl_6 and K_2YAuBr_6 halides.

3. Discussion of results

3.1. Structural characteristics

The crystal structure of the DPs ($A_2BB'X_6$) is almost the same as that of the single perovskites but with a double lattice parameter value. They have Fm $\bar{3}$ m space group. The Wyckoff positions of atoms in K_2YAuCl/Br_6 are: K atoms at 8*c*-site, Y atoms at 4*a*-site, Au atoms at 4*b*-site and Cl/Br atoms at 24*e*-site. The K and Y atoms are monovalent cations, and Au is trivalent while Cl/Br ions have oxidation state of −1 [43]. Figure 1 depicts the unit cell of K_2YAuCl/Br_6 DPs where it can be seen that purple-colored and green-colored balls correspond to K and Y atoms whereas golden and brown-colored balls correspond to Au and *X* atoms respectively. The energy-volume optimization graph of these DPs is shown in figure 2. The structural stability of K_2YAuCl_6 and K_2YAuBr_6 can be probed by calculating the tolerance factor (t_G) and thermodynamical stability can be checked by the calculation of enthalpy of formation (ΔH_f). The former term can be calculated using the atomic radii of all the atoms while the later term is measured using the energies of all the atoms. The expressions to compute both terms are given here [44]:

$$t_G = (r_K + r_X)/\sqrt{2}\,(r_B + r_X) \tag{1}$$

$$\Delta H_f = E_{\text{Total}}(K_a Y_b Au_c X_d) - aE_K - bE_Y - cE_{Au} - dE_X \tag{2}$$

Here r_K and r_X represent the atomic radii of K and X atoms and r_B represents the average atomic radii of Y and Au atoms. For stable structures, the t_G value reaches 1 as the range of t_G value for stable structures is between 0.8 to 1.4 [45]. The DPs under observation are structurally stable because the t_G values for K_2YAuCl_6 and K_2YAuBr_6 are 0.92 and 0.94, as listed in table 1, which lie within the stable range structures. The thermodynamical stability can be computed using equation (2) given above where $E_{\text{Total}}(K_a Y_b Au_c X_d)$ is the overall energy of the composition [45] and the terms E_K, E_Y, E_{Au} and E_X give energies of K, Y, Au and X atoms respectively. Every element has a different number of atoms that are represented by the coefficients a, b, c and d.

The value of ΔH_f for K_2YAuCl_6 and K_2YAuBr_6 are −2.08 eV and −1.56 eV, which are negative, so both compositions are thermally stable. Plotting the energy volume optimization graph leads to determine the optimized lattice parameters and bulk modulus value. All these computed parameters are presented in table 1, which show that lattice parameter (a_o) increased from 10.53 to 11.08 Å, and bulk modulus decreased from 35.52 to 30.03 GPa when Cl in the structure is replaced with Br. This variation in lattice parameter and bulk modulus is associated with relative ionic sizes of the host and substituent.

3.2. Mechanical characteristics

To probe the mechanical response of any material it is set under the mechanical stress and mechanical properties are determined in terms of elastic constants, which are fourth-order tensors. To compute these constants, the tensor matrix formed by the non-linear differential equations is solved. For the calculation of the mechanical response of cubic materials, one needs C_{11}, C_{12}, and C_{44} whose calculated values are given in table 1. The born stability criteria is verified based on the numerical values of these constants [47]. Here the substitution of Cl with

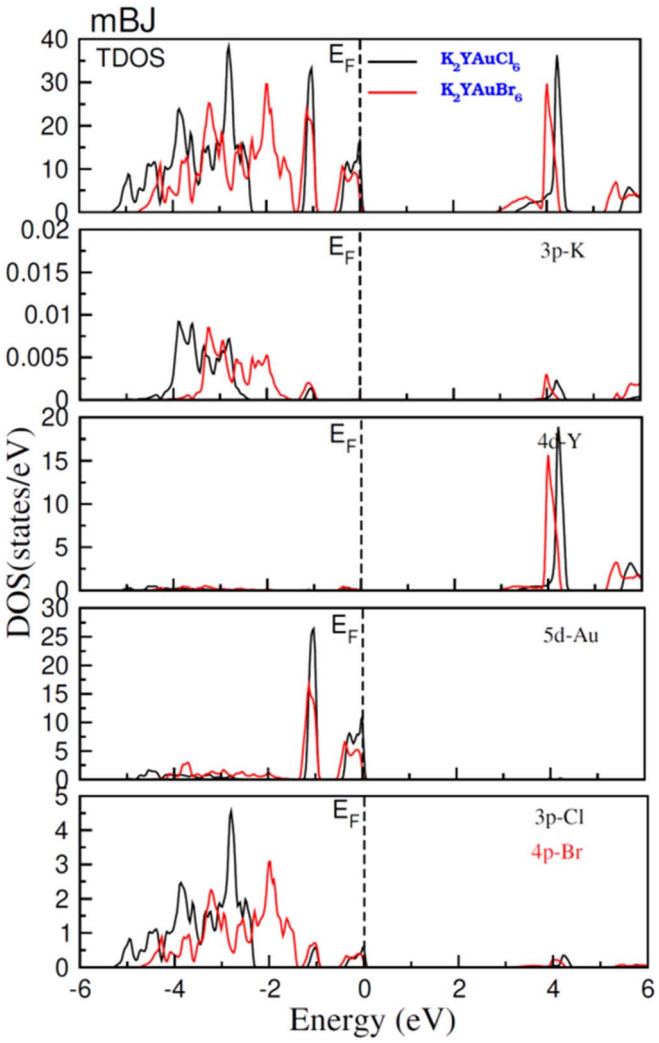

Figure 4. Calculated total density of stated (DOS) along with partial DOS for K_2YAuCl_6 and K_2YAuBr_6 halides.

Br causes the increase in lattice constant, which reduces the tensile strength and thus leads to the reduction in elastic modulus. The numerical values of these elastic moduli play a deterministic role in evaluating the material's brittle or ductile nature. Based on these modulus of elasticity values, two key parameters called Poisson's ratio (ν) and Pugh ratio (B/G) were computed. The realization of the ductile nature of the material is ascertained if the value of $B/G > 1.75$ or $\nu > 0.26$. In the current investigation, the value of G/B is 2.31 and 2.43 for K_2YAuCl_6 and K_2YAuBr_6, whereas the value of ν is 0.31 for both compositions, confirming the ductile nature of understudy materials [48].

In addition to calculating the elastic parameters, another exciting parameter called anisotropy constant (A) was also calculated, determining a fascinating aspect of the material. Anisotropy is one of the key features of crystalline materials where they give different response in different directions to any external stimulus [49]. Isotropic material is distinguished from anisotropic material from the value of their anisotropic constant which is 1 for isotropic materials. Any deviation from the unitary value indicates the anisotropic behavior of the material. The value of anisotropic constant for K_2YAuCl_6 and K_2YAuBr_6 is 0.20 and 0.35, respectively, which exhibited that that K_2YAuCl_6 is more anisotropic as compared to K_2YAuBr_6 .

3.3. Electronic characteristics

To ascertain the suitability of any material for optoelectronic devices, it is essential to map its bandgap structure. To probe the optoelectronic response of these double perovskites, we evaluated the electronic band structure using mBJ+SOC potential which is plotted in figure 3 [50]. The plotting of electronic band energy against different symmetry points revealed that the valence band maxima and conduction band minima lie at L, X-symmetry points respectively, exhibiting the indirect bandgap nature of these compositions [51]. The bandgap value for K_2YAuCl_6 is found to be 3.20 eV, which reduces to 2.70 eV when Cl is replaced with Br. This reduction in bandgap value is attributed to the larger atomic number and larger atomic size [52].

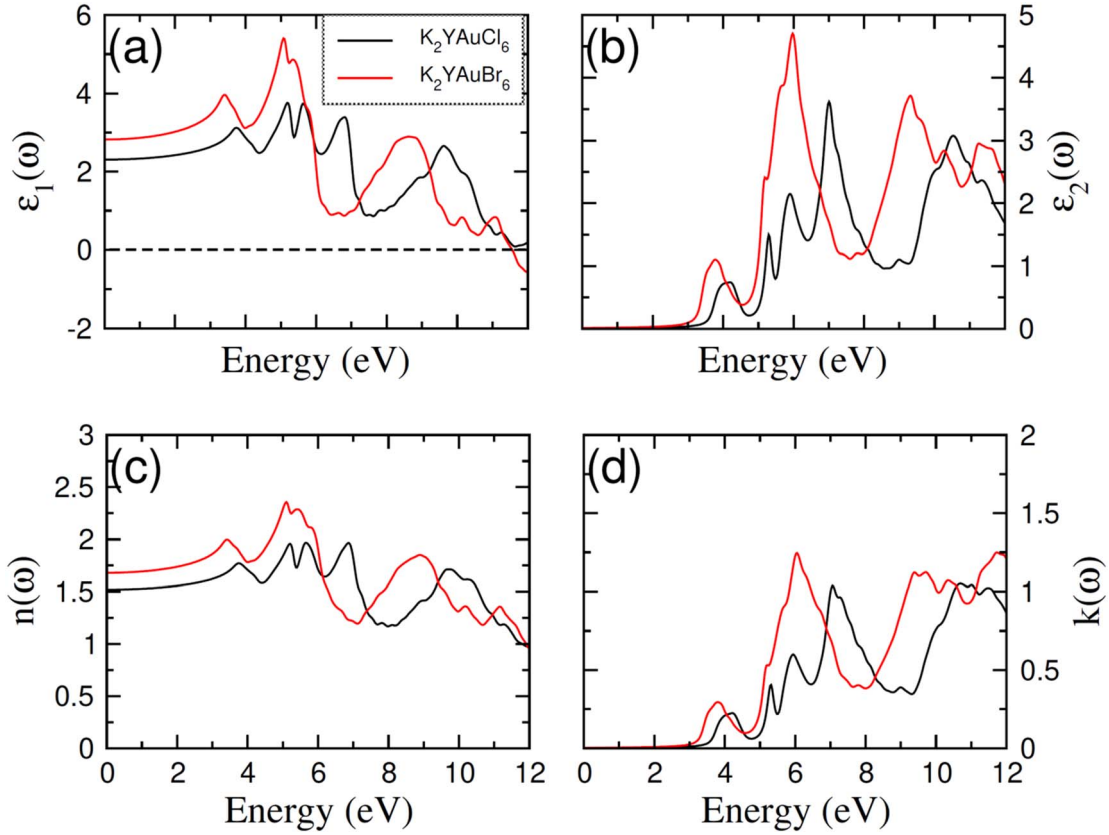

Figure 5. The calculated (a) real part $\varepsilon_1(\omega)$, (b) imaginary part $\varepsilon_1(\omega)$, (c) refractive index $n(\omega)$, (d) the extinction co-efficient $k(\omega)$ of K_2YAuCl_6 and K_2YAuBr_6 halides.

Table 2. Calculated direct bandgap E_g(eV) values with mBJ potential and optical parameters at 0 energy of K_2YAuCl_6 and K_2YAuBr_6 halides.

Parameters	K_2YAuCl_6	K_2YAuBr_6
	Our work	
E_g(eV)	3.20	2.70
$\varepsilon_1(0)$	2.31	2.82
n(0)	1.52	1.68
R(0)	0.04	0.06

The computation of the total (TDOS) and partial density of states (PDOS) gives a sound insight regarding the participation of different electronic states from various elements to forming electronic bands [53] and plots of TDOS and PDOS are presented in figure 4. This figure revealed that 3*p*-states of K significantly participated in the band formation, extending from −1 to −5 eV for K_2YAuCl_6 and −1 to −4 eV for K_2YAuBr_6. These states are deep in the conduction band and contribute a relatively small. In addition, 4*d*-states of Y are responsible for band formation and these states appear from 4 to 4.5 eV for K_2YAuCl_6 in the conduction band and slightly shifted towards the Fermi level for K_2YAuBr_6. These states are the closest to Fermi level in the conduction band and thus formed the conduction band edge. In the case of Au, 5*d*-states are contributing states in band formation, and they effectively do the job in valence band formation. In the valence band, they spread out from the Fermi level to −4.8 eV for K_2YAuCl_6 whereas these states are contracted towards Fermi level with increase of size of halogen. However, maximum density of states is around −0.9 to −1.2 eV. Moving to the halogen revealed that 3*p* and 4*p*-states of Cl and Br actively participated in valence band formation, and these states spread out in a wide energy range from Fermi level to −5.2 eV for K_2YAuCl_6 and Fermi level to −4.8 eV for K_2YAuBr_6 respectively [54].

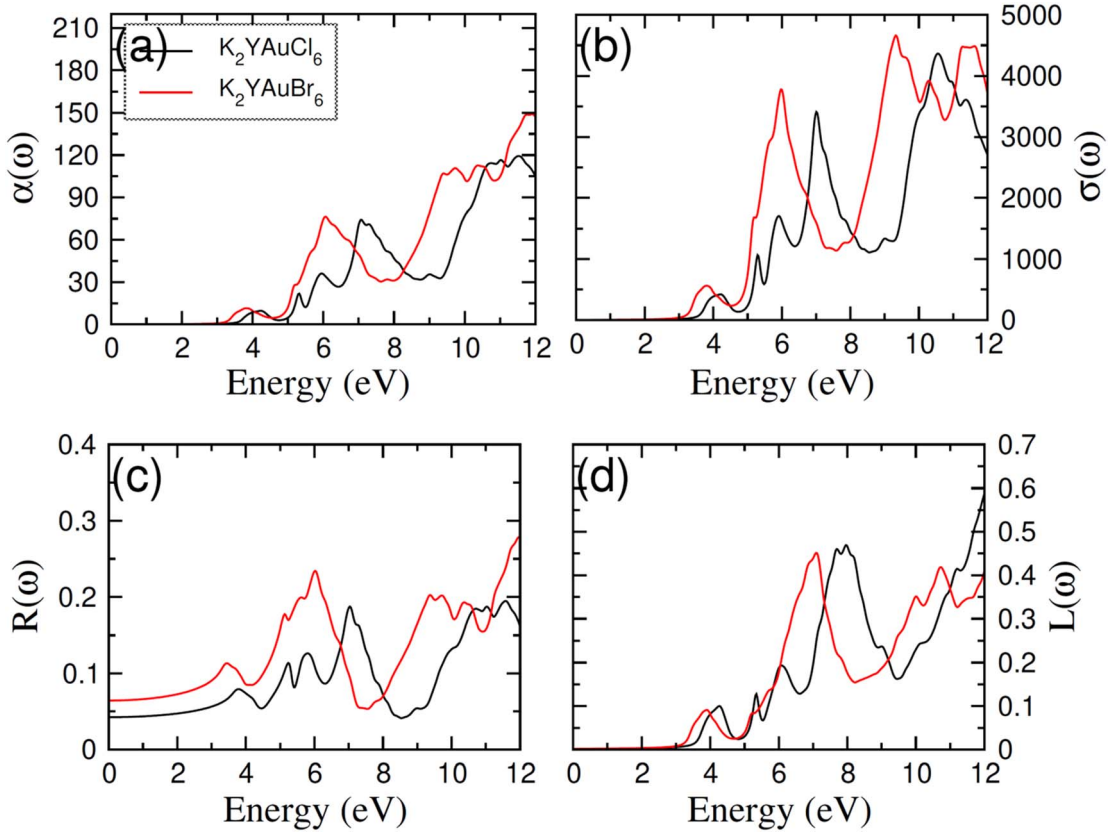

Figure 6. The calculated (a) absorption coefficient $\alpha(\omega)$, (b) optical conductivity, (c) reflectivity R(ω) and (d) energy loss L(ω) of K_2YAuCl_6 and K_2YAuBr_6 halides.

3.4. Optical characteristics

The optical behavior of any material depends upon the probability of inter-band electronic transitions and their recombination rate as well. The underlying mechanism behind the optical response of materials is the Kramer-Kronig relation which describes how matter reacts on exposure to external radiation [55]. This interaction is quantified in terms of various optical parameters such as real (ε_1) and imaginary (ε_2) parts of the dielectric constant which are plotted in figures 5(a) and (b). The $\varepsilon_1(\omega)$ quantifies the extent of polarization of the material as a result of interaction with radiation. The value of $\varepsilon_1(0)$ is known as the static dielectric constant and its value is found to be 2.31 and 2.82 for K_2YAuCl_6 and K_2YAuBr_6, respectively. The higher value of $\varepsilon_1(0)$ for Br-based composition indicates that Br-based composition is more polarizable which is because of the higher atomic size of Br as compared to Cl. This is due to the fact that the atomic polarizability is directly proportional to the size of the electronic cloud [56]. Since the size of the Br atom is larger as compared to Cl, this is why Br-based composition revealed higher value of $\varepsilon_1(0)$. Initially, $\varepsilon_1(\omega)$ raised with an increase of energy of interacting light and achieved the first maxima at 3.7 eV, the second maxima at 5.1 eV and these peaks are called relaxation peaks and are used to determine the resonance frequency. For K_2YAuBr_6, these peaks appeared at slightly lower energy value because of the involvement of heavier element Br as compared to K_2YAuCl_6. As a matter of fact, heavier masses have low resonance frequency. According to the Penny's model i.e., $\varepsilon_1(0) \approx 1 + (\hbar\omega_p/E_g)^2$, the $\varepsilon_1(0)$ is inversely linked with the bandgap value (E_g) which gives the extra support to the reduction of bandgap value of K_2YAuBr_6 [57].

During the interaction of electromagnetic radiations with matter, some part of the electromagnetic spectrum is absorbed, which is determined by $\varepsilon_2(\omega)$ and its variation is presented in figure 5(b). These spectra also help to determine the E_g value which are consistent with the bandgap values determined through electronic band structures. The peak value of $\varepsilon_2(\omega)$ appeared at 7 eV for K_2YAuCl_6, which reduced to 6 eV for K_2YAuBr_6, indicating that these materials are good absorbers for the ultraviolet region and their absorption range is almost constant. The value of refractive index at zero frequency n(0) is linked with $\varepsilon_1(0)$ as $n(0) = \sqrt{\varepsilon(0)}$. The value of n(0) for K_2YAuCl_6 and K_2YAuBr_6 are recorded as 1.52, and 1.68, respectively, as shown in table 2. The incidence of light on material's surface results in the multiple signals like reflection, absorption, and scattering. The incident light absorbs if energy of its photon is larger/equal to the material's bandgap, otherwise scatters [58]. In addition, the plot of extinction coefficient k(ω) shown in figure 5(d), also exhibited multiple peaks with the

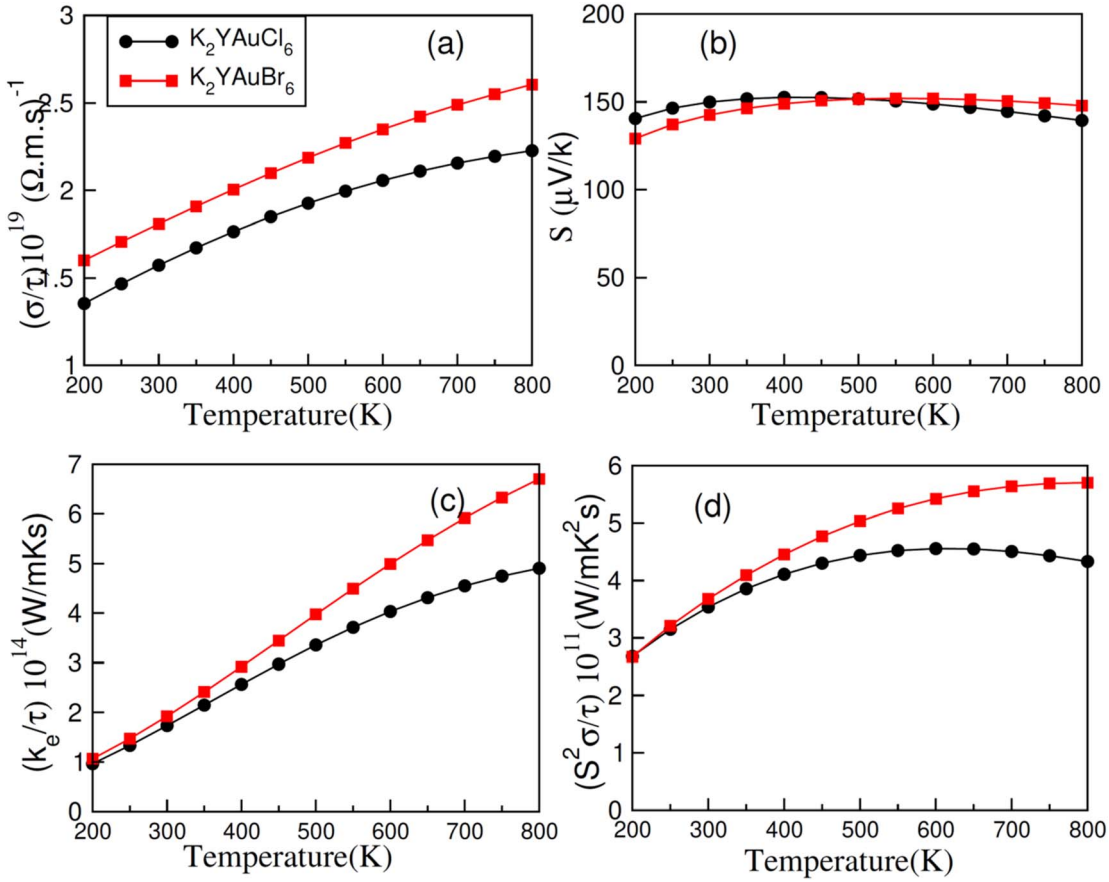

Figure 7. The calculated (a) electrical (σ/τ), (c) thermal (k_e/τ) conductivities, (b) Seebeck coefficient (S) and (d) power factor ($\sigma S^2/\tau$) of K_2YAuCl_6 and K_2YAuBr_6 against temperature (200 K–800 K).

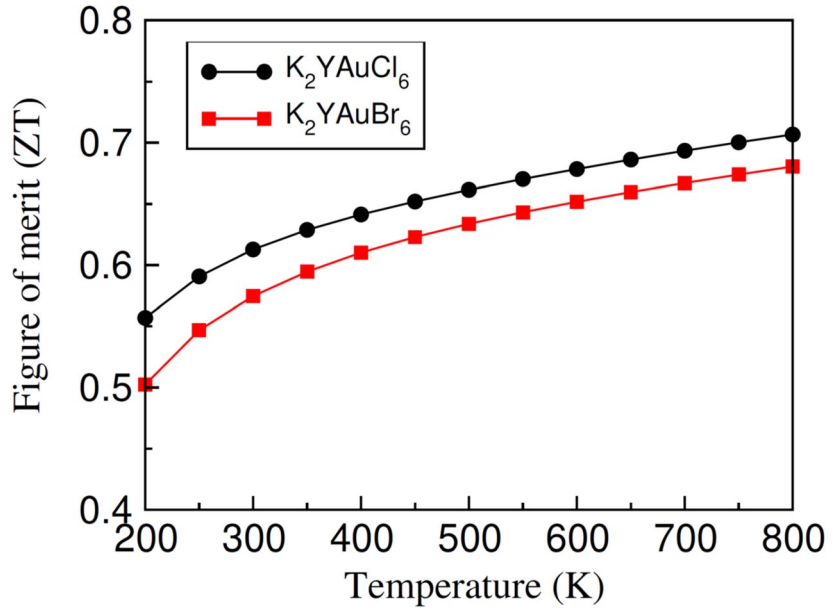

Figure 8. The calculated figure of merit (ZT) of K_2YAuCl_6 and K_2YAuBr_6 against temperature (200 K–800 K).

highest intensity peak appeared at 7.1 eV for K_2YAuCl_6, which is red shifted and emerged at 6 eV for K_2YAuBr_6. The position of these peaks in this graph is identical to the $\varepsilon_2(\omega)$ graph which is presented in part (b).

Absorption coefficient $\alpha(\omega)$ is another key factor which quantifies the amount of energy absorbed per unit length and its variation with energy of incident EM radiation is plotted in figure 6(a) [59]. The high value of $\alpha(\omega)$

Table 3. Comparison of thermoelectric parameters of under study compositions with literature at room temperature.

Compositions	$\sigma/\tau(\times 10^{19}/\Omega ms)$	$\kappa_e/\tau(\times 10^{19}/\Omega ms)$	S (μV/K)	ZT	References
Rb_2YInCl_6	1.57	0.36	242.35	0.76	[70]
Rb_2YInBr_6	1.53	0.34	234.17	0.74	[70]
K_2YAgBr_6	1.65	1.98	158.48	0.63	[71]
K_2YAgI_6	0.95	1.64	158.48	0.74	[71]
K_2YAuCl_6	1.55	1.80	151.02	0.62	This work
K_2YAuBr_6	1.75	1.95	145.17	0.57	This work

corresponds to better interband electronic transitions [60]. The flow of charge particles in the presence of electromagnetic field is coined as the optical conductivity $\sigma(\omega)$. It varies with frequency of applied field and its variation is presented in figure 6(b). It appeared minimum in the same region of the electromagnetic spectrum where $\alpha(\omega)$ was minimum [61]. Each composition exhibited two high-intensity peaks in the UV region. For K_2YAuCl_6, these peaks appeared at 7.0 eV and 10.5 eV whereas for K_2YAuBr_6, these peaks are red-shifted (towards low energy) and emerged at 6.0 eV and 9.3 eV. The presence of these peaks in UV region stipulates their utilization for optoelectronic devices working in UV regions like Mercury lamps and plasma torches [62]. Interestingly, the height of peaks corresponding to K_2YAuBr_6 spectrum is larger which is due to the larger number of electrons preset in this composition. Figure 6(c) shows the variation of optical reflectivity R(ω) at zero hertz frequency R(0) and its value is observed as 0.04 and 0.06 for K_2YAuCl_6 and K_2YAuBr_6, respectively [63]. The large value of R(0) for K_2YAuBr_6 is because of the high atomic number and larger electronic density of Br as compared to Cl. During motion inside the material, the energy of electrons decay which is measured by the optical loss function L (ω), and that is presented in figure 6(d). The peaks in these spectra correspond to the plasma resonance of materials. The phenomenon of collective vibration of valence band electrons is termed as plasma resonance and associated frequency is known as plasma frequency (ω_p) [64]. The significant peaks in L (ω) appeared in UV region at 8 eV and 7 eV for K_2YAuCl_6 and K_2YAuBr_6 respectively.

3.5. Thermoelectric properties

The concept of Seebeck and Peltier effect emerged back in 19th century which opened new horizons for energy harvesting technology. By their capacity of mutual conversion of thermal and electrical energy thermoelectric materials are capable to revolutionize modern-day technology like semiconductor refrigeration and waste heat recovery. Researchers have always intended to expand the scope and area of applications of thermoelectric materials by improving their thermoelectric efficiency. The thermoelectric efficiency of any material is indexed by the unitless figure of merit (ZT), which is equal to $S^2\sigma T/\kappa$ [65]. The variation of temperature-dependent electrical conductivity (σ/τ) is presented in figure 7(a) in the temperature range of 200–800 K. Here τ represent the relaxation time, and its value lies in the range of 10^{-13}–10^{-14} s for most semiconducting materials. In the present scenario, for calculating thermoelectric properties, we set its value as 10^{-14} s [66]. At 200 K, the value of σ/τ was recorded as 1.35 and 1.65 $\times 10^{19}$ $(\Omega ms)^{-1}$ for K_2YAuCl_6 and K_2YAuBr_6, respectively. With increase of temperature (T), a linear increase in σ/τ was observed and it reached to 2.12 and 2.61 $\times 10^{19}$ $(\Omega ms)^{-1}$ at 800 K. In addition to σ/τ, the electronic part of thermal conductivity (κ_e/τ) is plotted in figure 7(c). Since Boltztrap code cannot take into account the lattice part of thermal conductivity κ_l/τ due to which only electronic part was considered here. The value of κ_e/τ was noticed as 1×10^{14} W/mKs for both materials at 200 K and increased with temperature [67]. The rate of increase for K_2YAuBr_6 is greater due to which the value of κ_e/τ for this composition reached to 6.7×10^{14} W $mK^{-1}s^{-1}$ at 800 K whereas the for K_2YAuCl_6 this value is noticed as 4.8×10^{14} W $mK^{-1}s^{-1}$. This larger value of κ_e/τ for K_2YAuBr_6 may be due to this composition's greater mobility and high carrier concentration. The calculation of Seebeck coefficient was executed and computed values are plotted in figure 7(b). The positive value of S indicates the presence of positive charge carriers. In the studied range of temperature, S varied slightly in the 130–150 μV K^{-1} range. For potentially active thermoelectric materials, the value of S lies in the range of 200 μV K^{-1} [68]. Thermoelectric materials' efficiency is mapped by calculating the value of power factor (PF) or figure of merit (ZT). These two parameters differ from each other on the basis of the inclusion or exclusion of thermal conductivity. PF estimates the conversion efficiency without taking into account κ/τ whereas ZT take its effect, this is why efficiency determined by the ZT is more accurate as compared with PF. The calculated value of PF is plotted in figure 7(d), having value 2.7×10^{11} W mK^2s at 200 K for both compositions and increased to 4.4×10^{11} and 5.7×10^{11} W mK^2s at 800 K for K_2YAuCl_6 and K_2YAuBr_6 respectively. The most significant parameter in the estimation of the thermoelectric response of the material is ZT which is expressed in figure 8. Its value was noticed as 0.55 and 0.50 at 200 K and .71 and 0.68 at 800 K for K_2YAuCl_6 and K_2YAuBr_6 respectively. This trend of this graph shows that the value of ZT can further be

improved by increasing the temperature, making these compositions suitable for high-temperature applications [69]. A comparison of thermoelectric parameters of different double perovskites is presented in the table 3.

4. Conclusion

In nutshell, we elaborated here the structural, optical, electronic, and transport properties of K_2YAuX_6 (X = Cl, Br) double perovskites using the WIEN2K code. In this study, the structure was first relaxed to determine the optimized lattice parameters and ground state energy. The computation of elastic constants, modulus of elasticity, and Poisson's (>0.26) and Pugh (>1.75) ratios confirmed their ductile nature. The electronic band structure revealed the in-direct bandgap nature with bandgap values of 3.20 eV and 2.82 eV for K_2YAuCl_6 and K_2YAuBr_6 respectively. The analysis of the total density of states and partial density of states provided a clear picture regarding the contribution of various states of involving atoms. The presence of multiple peaks in UV region for dielectric constant, refractive index, optical conductivity, and absorption spectra gave a clue about the range of applicability of these compositions. The high value of the Wiedemann–Franz ratio, large electrical conductivity, and Seebeck coefficient with a small value of thermal conductivity highlighted the importance of these compositions for futuristic thermoelectric devices.

Acknowledgments

The authors would like to acknowledge Researcher's Supporting Project Number (RSP2023R511), King Saud University, Riyadh, Saudi Arabia.

Data availability statement

All data that support the findings of this study are included within the article (and any supplementary files).

ORCID iDs

Muhammad Imran https://orcid.org/0000-0003-3137-2918

References

[1] Wu Y, Li Y, Long Y, Xu Y, Yang J, Zhu H and Shi G 2022 High-efficiency photo-thermo-electric system with waste heat utilization and energy storage *ACS Appl. Mater. Interfaces* **14** 40437–46
[2] Hooshmand Zaferani S, Jafarian M, Vashaee D and Ghomashchi R 2021 Thermal management systems and waste heat recycling by thermoelectric generators—an overview *Energies* **14** 5646
[3] Koumoto K and Mori T 2013 Thermoelectric nanomaterials *Materials Design and Applications, Springer Series in Materials Science* **182** 1–382
[4] Bu Z, Zhang X, Hu Y, Chen Z, Lin S, Li W and Pei Y 2022 A record thermoelectric efficiency in tellurium-free modules for low-grade waste heat recovery *Nat. Commun.* **13** 1–8
[5] Cao T, Shi X L and Chen Z G 2022 Advances in the design and assembly of flexible thermoelectric device *Prog. Mater Sci.* **131** 101003
[6] Zhang Q, Deng K, Wilkens L, Reith H and Nielsch K 2022 Micro-thermoelectric devices *Nat. Electron.* **5** 333–47
[7] Wu Z, Zhang S, Liu Z, Mu E and Hu Z 2022 Thermoelectric converter: strategies from materials to device application *Nano Energy* **91** 106692
[8] Yang X, Wang C, Lu R, Shen Y, Zhao H, Li J and Zheng X 2022 Progress in measurement of thermoelectric properties of micro/nano thermoelectric materials: a critical review *Nano Energy* **101** 107553
[9] Berri S and Bouarissa N 2022 Probable thermoelectric materials for promising candidate of optoelectronics for Ba-based complex perovskite compounds *Int. J. Energy Res.* **46** 9968–84
[10] Yan Q and Kanatzidis M G 2022 High-performance thermoelectrics and challenges for practical devices *Nat. Mater.* **21** 503–13
[11] Jaafreh R, Seong K Y, Kim J G and Hamad K 2022 A deep learning perspective into the figure-of-merit of thermoelectric materials *Mater. Lett.* **319** 132299
[12] Song D, Chi C, An M, Du Y, Ma W, Wang K and Zhang X 2022 Ionic seebeck coefficient and figure of merit in ionic thermoelectric materials *Cell Reports Physical Science* **3** 101018
[13] Huang S, Ning S and Xiong R 2022 First-principles study of silicon–tin alloys as a high-temperature thermoelectric material *Materials* **15** 4107
[14] Lin S, Zhang L, Zeng W, Shi D, Liu S, Ding X and Tao X 2022 Flexible thermoelectric generator with high Seebeck coefficients made from polymer composites and heat-sink fabrics *Communications Materials* **3** 1–13
[15] Pan Y, Lin B and Chen J 2007 Performance analysis and parametric optimal design of an irreversible multi-couple thermoelectric refrigerator under various operating conditions *Appl. Energy* **84** 882–92
[16] Osterhage H, Gooth J, Hamdou B, Gwozdz P, Zierold R and Nielsch K 2014 Thermoelectric properties of topological insulator Bi2Te3, Sb2Te3, and Bi2Se3 thin film quantum wells *Appl. Phys. Lett.* **105** 123117
[17] Xia Q, Xu Q, Xu B and Yi L 2021 *Ab initio* prediction of thermoelectric performance of monolayer BiSbTe3 *J. Solid State Chem.* **296** 121963

[18] Radja K, Farah B L, Ibrahim A, Lamia D, Fatima I, Nabil B and Abd El-Rehim A F 2022 Investigation of structural, magneto-electronic, elastic, mechanical and thermoelectric properties of novel lead-free halide double perovskite Cs2AgFeCl6: first-principles calcuations *J. Phys. Chem. Solids* **167** 110795

[19] Kung P K, Li M H, Lin P Y, Jhang J Y, Pantaler M, Lupascu D C and Chen P 2020 Lead-free double perovskites for perovskite solar cells *Sol. RRL* **4** 1900306

[20] King G and Woodward P M 2010 Cation ordering in perovskites *J. Mater. Chem.* **20** 5785–96

[21] Akkerman Q A and Manna L 2020 What defines a halide perovskite? *ACS Energy Lett.* **5** 604–10

[22] Fu W T and IJdo D J W 2005 On the space group of the double perovskite Ba2PrIrO6 *J. Solid State Chem.* **178** 1312–6

[23] Yang J, Dai J, Liu Z, Yu R, Hojo H, Hu Z and Long Y 2017 High-pressure synthesis of the cobalt pyrochlore oxide Pb2Co2O7 with large cation mixed occupancy *Inorg. Chem.* **56** 11676–80

[24] Yamamura K, Wakeshima M and Hinatsu Y 2006 Structural phase transition and magnetic properties of double perovskites Ba2CaMO6 (M = W, Re, Os) *J. Solid State Chem.* **179** 605–12

[25] Sederholm L, Tiittanen T and Karppinen M 2023 High-pressure stabilisation of R = Y member of R2CuTiO6 double perovskite series *J. Solid State Chem.* **317** 123646

[26] Al-Muhimeed T I, Aljameel A I, Mera A, Saad S, Nazir G, Albalawi H and Mahmood Q 2022 First principle study of optoelectronic and mechanical properties of lead-free double perovskites Cs2SeX6 (X = Cl, Br, I) *Journal of Taibah University for Science* **16** 155–62

[27] Bartel C J, Clary J M, Sutton C, Vigil-Fowler D, Goldsmith B R, Holder A M and Musgrave C B 2020 Inorganic halide double perovskites with optoelectronic properties modulated by sublattice mixing *JACS* **142** 5135–45

[28] Kattan N A, Rouf S A, Sfina N, Mana Al-Anazy M, Ullah H, Hakamy A and Amin M A 2023 Tuning of band gap by anion variation of double perovskites K2AgInX6 (X= Cl, Br) for solar cells and thermoelectric applications *J. Solid State Chem.* **319** 123820

[29] Kangsabanik J, Sugathan V, Yadav A, Yella A and Alam A 2018 Double perovskites overtaking the single perovskites: a set of new solar harvesting materials with much higher stability and efficiency *Phys. Rev. Mater.* **2** 055401

[30] Chakraborty S *et al* 2017 Rational design: a high-throughput computational screening and experimental validation methodology for lead-free and emergent hybrid perovskites *ACS Energy Lett.* **2** 837–45

[31] Slavney A H, Hu T, Lindenberg A M and Karunadasa H I 2016 A bismuth-halide double perovskite with long carrier recombination lifetime for photovoltaic applications *J. Am. Chem. Soc.* **138** 2138–41

[32] Volonakis G *et al* 2017 $Cs_2InAgCl_6$: a new lead-freehalide double perovskite with direct band gap *J. Phys. Chem. Lett.* **8** 772–8

[33] Meng W, Wang X, Xiao Z, Wang J, Mitzi D B and Yan Y 2017 Parity-forbidden transitions, and their impact on the optical absorption properties of lead-free metal halide perovskites and double perovskites *J. Phys. Chem. Lett.* **8** 2999–3007

[34] Blaha P, Schwarz W, Madsen G K H, Kvasnicka D and Luitz J 2001 An Augmented Plane Wave +Local Orbitals Program for Calculating Crystal Properties, Karlheinz Schwarz, Techn, Universitat Wien, Austria. WIEN2K

[35] Blaha P, Schwarz K, Sorantin P and Trickey S K 1990 Full potential, linearized augmented plane wave programs for crystalline systems *Compu Phys Commun.* **59** 339

[36] Madsen G K H, Schwarz K and Singh D J 2006 BoltzTraP. a code for calculating band- structure dependent quantities *Comput. Phys. Commun.* **175** 67

[37] Fuchizaki K 2006 Murnaghan's equation of state revisited *J. Phys. Soc. Jpn.* **75** 034601

[38] Tran F and Blaha P 2009 Accurate band gaps of semiconductors and insulators with a semi-local exchange-correlation potential *Phys. Rev. Lett.* **102** 226401

[39] Koller D, Tran F and Blaha P 2011 Merits and limits of the modified Becke-Johnson exchange potential *Phys. Rev.* B **83** 195134

[40] Jiang S, Fang Y, Li R *et al* 2016 Pressure-dependent polymorphism and band-gap tuning of methyl ammonium lead iodide perovskites *Angew. Chem. Int. Ed.* **55** 6540

[41] Singh N, Anjum D, Das G, Qattan I, Patole S and Sajjad M 2020 Phonon dynamics and transport properties of copper thiocyanate and copper selenocyanate pseudo-halides *ACS Omega.* **5** 28637–42

[42] Singh D, Sajjad M, Larsson J A and Ahuja R 2020 Promising high-temperature thermoelectric response of bismuth oxybromide *Results Phys.* **19** 103584

[43] Bartel1 C J *et al* 2019 New tolerance factor to predict the stability of perovskite oxides and halides *Sci. Adv.* **5** 693

[44] Young J and Rondinelli J 2016 Octahedral rotation preferences in perovskite iodides and bromides *Phys. Chem. Lett.* **7** 918–22

[45] Fedorovskiy A E, Drigo N A and Nazeeruddin M K 2020 The Role of Goldschmidt's tolerance factor in the formation of A_2BX_6 double Halide perovskites and its optimal range *Small Meth.* **4** 1900426

[46] Jain A *et al* 2013 Commentary: the materials project: a materials genome approach to accelerating materials innovation *APL Mater.* **1** 011002

[47] Hussain M, Rashid M, Ali A, Bhopal M F and Bhatti A S 2020 Systematic study of optoelectronic and transport properties of cesium lead halide (Cs2PbX6; X = Cl, Br, I) double perovskites for solar cell applications *Ceram. Int.* **46** 21378–87

[48] Hu D Y, Zhao X H, Tang T Y, Lu L M, Li L, Gao L K and Tang Y L 2021 First-principles study on the structural, elastic, electronic and optical properties of lead-free double perovskites Cs2CuBiX6 (XI, Br, Cl) *Materials Today Communications* **29** 102842

[49] Katayama T, Chikamatsu A, Zhang Y, Yasui S, Wadati H and Hasegawa T 2021 Ionic order engineering in double-perovskite cobaltite *Chem. Mater.* **33** 5675–80

[50] Gabrelian B V, Lavrentyev A A, Vu T V, Tkach V A, Marchuk O V, Kalmykova K F and Khyzhun O Y 2020 Quaternary Cu2HgGeSe4 selenide: its electronic and optical properties as elucidated from TB-mBJ band-structure calculations and XPS and XES measurements *Chem. Phys.* **536** 110821

[51] Yuan L D, Deng H X, Li S S, Wei S H and Luo J W 2018 Unified theory of direct or indirect band-gap nature of conventional semiconductors *Phys. Rev.* B **98** 245203

[52] Li Z, Kavanagh S R, Napari M, Palgrave R G, Abdi-Jalebi M, Andaji-Garmaroudi Z and Hoye R L 2020 Bandgap lowering in mixed alloys of Cs 2 Ag (Sb x Bi 1 − x) Br 6 double perovskite thin films *J. Mater. Chem.* **8** 21780–8

[53] Din M U, Munir J, Jamil M, Saeed M A and Ain Q 2022 Electronic structure and optical response of double perovskite Rb2NaCoF6 for optoelectronic devices *Physica* B **627** 413533

[54] Idrissi S, Ziti S, Labrim H and Bahmad L 2021 Band gaps of the solar perovskites photovoltaic CsXCl3 (X = Sn, Pb or Ge) *Mater. Sci. Semicond. Process.* **122** 105484

[55] Baek Y and Park Y 2021 Intensity-based holographic imaging via space-domain Kramers–Kronig relations *Nat. Photonics* **15** 354–60

[56] Bijelić J, Tatar D, Hajra S, Sahu M, Kim S J, Jagličić Z and Djerdj I 2020 Nanocrystalline antiferromagnetic high-κ dielectric Sr2NiMO6 (M = Te, W) with double perovskite structure type *Molecules* **25** 3996

[57] Ticha H and Tichy L 2022 Remark on the correlation between the refractive index and the optical band gap in some crystalline solids *Mater. Chem. Phys.* 126949

[58] Nishizawa N, Hamada A, Takahashi K, Kuchimaru T and Munekata H 2020 Monte Carlo simulation of scattered circularly polarized light in biological tissues for detection technique of abnormal tissues using spin-polarized light emitting diodes *Jpn. J. Appl. Phys.* **59** SEEG03
[59] Wang Z Y, Chen Y, Zhang C, Wang D, Liang P, Zhang H and Wang L 2020 Electronic structure and optical properties of vacancy-ordered double perovskites Cs2Pd Br x Cl6–x by first-principles calculation *J. Phys. Chem.* **124** 13310–5
[60] Soni Y, Rani U, Shukla A, Joshi T K and Verma A S 2022 Transition metal-based halides double Cs2ZSbX6 (Z = Ag, Cu, and X = Cl, Br, I) perovskites: a mechanically stable and highly absorptive materials for photovoltaic devices *J. Solid State Chem.* **314** 123420
[61] Roknuzzaman M, Zhang C, Ostrikov K K, Du A, Wang H, Wang L and Tesfamichael T 2019 Electronic and optical properties of lead-free hybrid double perovskites for photovoltaic and optoelectronic applications *Sci. Rep.* **9** 1–7
[62] Wang Q, Gong Z, Wu S, Pan S and Pan J 2022 UV photodetector properties of CsPbCl3 grown by Vertical Bridgman method *J. Cryst. Growth* **596** 126838
[63] Haid S, Benstaali W, Abbad A, Bouadjemi B, Bentata S and Aziz Z 2019 Thermoelectric, structural, optoelectronic and magnetic properties of double perovskite Sr2CrTaO6: first principle study *Materials Science and Engineering:* B **245** 68–74
[64] Alotaibi N H, Mustafa G M, Kattan N A, Mahmood Q, Albalawi H, Morsi M and Amin M A 2022 DFT study of double perovskites Cs2AgBiX6 (X = Cl, Br): an alternative of hybrid perovskites *J. Solid State Chem.* **313** 123353
[65] Mir S A and Gupta D C 2021 Understanding the origin of semiconducting ferromagnetic character along with the high figure of merit in Cs2NaMCl6 (M = Cr, Fe) double perovskites *J. Magn. Magn. Mater.* **519** 167431
[66] Li Y F, Tang G H and Fu B 2019 Hydrogenation: an effective strategy to improve the thermoelectric properties of multilayer silicene *Phys. Rev.* B **99** 235428
[67] Klarbring J, Hellman O, Abrikosov I A and Simak S I 2020 Anharmonicity and ultralow thermal conductivity in lead-free halide double perovskites *Phys. Rev. Lett.* **125** 045701
[68] Prenninger P, Grytsiv A, Rogl P and Bauer E 2009 12 Thermo-electric-materials with better efficiencies *Thermoelektrik* **94** 124
[69] Wolf M, Hinterding R and Feldhoff A 2019 High power factor vs. high zT—A review of thermoelectric materials for high-temperature application *Entropy* **21** 1058
[70] Nawaz P A, Mustafa G M, Iqbal S S, Noor N A, Ahmad T S, Mahmood A and Neffati R 2022 Theoretical investigations of optoelectronic and transport properties of Rb_2YInX_6 (X = Cl, Br, I) double perovskite materials for solar cell applications *Sol. Energy* **231** 586–92
[71] Mustafa G M, Slam A, Saba S, Noor N A, Iqbal M W and Dahshan A 2023 Optoelectronic and thermoelectric characteristics of halide based double perovskites K_2YAgX_6 (X = Br, I) for energy storage applications *Polyhedron* **229** 116184